

## Simulation of turbulent flow of turbine passage with uniform rotating velocity of guide vane

Wen-Quan Wang\* and Yan Yan

*Department of Engineering Mechanics, Kunming University of Science and Technology,  
Kunming 650500, China*

*(Received December 4, 2017, Revised January 30, 2018, Accepted January 31, 2018)*

**Abstract.** In this study, a computational method for wall shear stress combined with an implicit direct-forcing immersed boundary method is presented. Near the immersed boundaries, the sub-grid stress is determined by a wall model in which the wall shear stress is directly calculated from the Lagrangian force on the immersed boundary. A coupling mathematical model of the transition process for a model Francis turbine comprising turbulent flow and rotating rigid guide vanes is established. The spatiotemporal distributions of pressure, velocity, vorticity and turbulent quantity are gained with the transient process; the drag and lift coefficients as well as other forces (moments) are also obtained as functions of the attack angle. At the same time, analysis is conducted of the characteristics of pressure pulsation, velocity stripes and vortex structure at some key parts of flowing passage. The coupling relations among the turbulent flow, the dynamical force (moment) response of blade and the rotating of guide vane are also obtained.

**Keywords:** immersed boundary method; velocity correction; large eddy simulation; turbulent flow; transition process; hydraulic turbine

---

### 1. Introduction

Transient processes in hydraulic turbines are transitions from one operating point to another, controlled by the rotation of a guide vane as well as valves or wicket gates opening upstream, the application of a payload to the generator, or other means. Examples of such processes are power increase/decrease, runaway and emergency turbine shutdown. The majority pass far from the best efficiency point in areas of unstable operation, where strong unsteadiness of the flow is observed (Wang *et al.* 2010, Cherny *et al.* 2010, Li *et al.* 2010). Moreover, most of the transient processes are associated with significant discharge changes, causing water hammer waves that travel back and forth through the whole water system. Furthermore, vortices shed around the rotating guide vane may enter into the runner blade passage and often induces strong vibration of the unit (Gorla *et al.* 2005, Jiang *et al.* 2010, Zhang *et al.* 2010, Wang *et al.* 2010). These characteristics of transient processes make the task of simulating them rather complex.

Nowadays, the most robust approach to investigating transient behaviour in hydroelectric plants

---

\*Corresponding author, E-mail: [wqwangkm@126.com](mailto:wqwangkm@126.com)

is one-dimensional (1D) hydro-acoustic theory. It is based on a hyperbolic system of mass and momentum continuity equations for compressible fluid (Nicolet 2007). In frames of this approach and with the aid of an analogy to electricity, one can consider branched pipe systems and take into account all basic components of hydro power plants, including surge tanks and valves, using modelling software such as SIMSEN or WANDA soft. The turbine itself is represented by its equivalent hydraulic resistance and inductance, taken from a turbine efficiency hill-chart. Therefore, the application of this approach requires the turbine hill-chart to be known a priori. A 1D approach cannot be used to describe and simulate unsteady three-dimensional (3D) flow structures such as vortices, re-circulations and cavitation, arising in flow passages at the transients. One way to overcome this difficulty is to assume that the instantaneous flow field behaviour in a given moment of a transient process is the same as its behaviour in a corresponding stationary operating point of a steady state hill-chart. However, this is not quite true in reality. Meanwhile, some multi-dimensional mathematical models have been developed (such as one combining 1D and 3D models (Chirkov *et al.* 2012, Zhang *et al.* 2012), some research on transient processes in particular cases has been undertaken and some control strategies have also been proposed (De *et al.* 1994, Alligné *et al.* 2010, Nicolle *et al.* 2012).

On the other hand, the last two decades have seen the development of CFD models and algorithms that have well-advanced simulation of steady and unsteady 3D turbulent flows in hydraulic machines. Simulation of these flows, as well as some experimental testing of the transient processes in hydraulic machines, has attracted considerable attention (Werner and Peter 2004, Keck and Sick 2008, Jain and Patel 2014), e.g., there have been studies on the instability in pump turbines caused by the pump's hump area (Li *et al.* 2015), rotating stall (Liu *et al.* 2013a) and the 'S'-type area formed during turbine braking (Liu *et al.* 2013b, Yin *et al.* 2014, Widmer *et al.* 2011). There are two main methods of simulating the transient process: one is simulation of steady flow at different openings of the guide vane (Hasmatuchi *et al.* 2011, Olimstad *et al.* 2012) and the other is simulation of unsteady flow with re-mesh technology. The traditional method comprises straightforward domain-time discretisation with accurate and efficient numerical algorithms, and it usually achieves good results when considering simple model problems in trivial geometries. In fact, relevant turbulent flows in hydraulic turbines always occur in very complex geometries in which the computation becomes more involved and less efficient, sometimes even failing owing to the presence of a body-conformal grid or dynamical mesh. Traditional body-fitted numerical methods, which strongly couple the solution of governing equations and implementation of boundary conditions, usually need tedious grid generation from the solid boundary. These arguments support the common statement that adequate treatment of complex geometric configurations is one of the main obstacles facing the application of CFD as a standard design tool in the industry, so adaptive fixed mesh methods with solved algorithms have attracted many researchers in recent years; one of these methods is the immersed boundary (IB) method.

The IB method was first introduced by Peskin (1972) in the simulation of blood flow around the flexible leaflet of a human heart. Some reviews of the IB method include Mittal *et al.* (2005) and Peskin (2003), as well as Sotiropoulos *et al.* (2014). In the framework of the IB method, the fluid motion equations are discretised on a fixed Cartesian grid which, in general, does not conform to the geometry of moving structures. As a result, interaction between the fluid and the solid is achieved by information transfer between the IB and Cartesian grid points.

In this study, we focus on the use of the traditional turbulence wall model combined with the immersed boundary method for the simulation of complex turbulent flows. The governing equations are discretised in space using a finite volume method on a hybrid non-staggered grid

(Gilmanov and Sotiropoulos 2005, Kang *et al.* 2011) and integrated in time using an efficient fractional step method. In fact, while many direct numerical simulations and LESs have been performed using IB methods, much less work has been done on the classical turbulent model, which is better suited for complex turbulent flow in hydraulic turbine-engineering applications. We also present a new velocity correction and wall shear stress computational strategy, which iteratively computes the immersed body force distribution and ad hoc corrections of the near-wall solution until the no-slip wall condition is satisfied.

The study is organised as follows: the governing equations and turbulent model will be simply introduced in Section 2.1 with regard to their relation to the IB method. The time-advanced approach with velocity correction will be presented in Section 2.2. Then, the new simple computational method for wall stress in the near-wall model that we employ will be briefly described in Section 2.3. An illustrative example, namely, the transition process of a hydraulic turbine with a continuously rotating guide vane, will then be discussed in Section 3 in order to show the concepts previously introduced in real applications. In Section 4, we will present the conclusions of this study and discuss areas for future research.

## 2. Methodology

### 2.1 Governing equations

Consider the problem of a viscous incompressible fluid in a rectangular domain ( $\mathbf{X}$ ) containing an immersed, massless boundary in the form of a simple closed curve (2D) or surface (3D)  $\Gamma$ , as shown in Fig. 1. It is clear from this figure that few, if any, of the points comprising  $\Gamma$  coincide with grid points.

As mentioned above, the influence of the immersed boundary on the fluid is represented by the forces exerted on the fluid to impose the no-slip condition at the immersed boundary. Therefore, the governing equations of this fluid-structure interaction system are the usual incompressible Navier-Stokes equations. Since turbulent flow is considered here, the large eddy simulation (LES) technique is adopted to model turbulence. Thus, the grid-filtered, incompressible continuity and Navier-Stokes equations take the following forms

$$\frac{\partial u_i}{\partial x_i} = 0 \quad (1)$$

$$\begin{aligned} \frac{\partial \rho u_i}{\partial t} + \frac{\partial (\rho u_i u_j)}{\partial x_j} = & -\frac{\partial p}{\partial x_i} + \frac{\partial}{\partial x_j} \left[ \mu \left( \frac{\partial u_i}{\partial x_j} + \frac{\partial u_j}{\partial x_i} \right) \right] \\ & - \frac{\partial \tau_{ij}}{\partial x_j} + f_i \end{aligned} \quad (2)$$

where  $u_i$  and  $p$  are the grid-filtered velocity and pressure, respectively.  $\rho$  is the fluid density,  $\mu$  is the dynamic viscosity, and  $\tau_{ij}$  are the sub-grid stresses that are not resolved by the computational grids and have to be modelled. For laminar flow, the  $\tau_{ij}$  values are zero. The boundary body force density term,  $f_i$ , can be expressed as

$$f_i(\mathbf{x}, t) = \int_{V_i} F_i(\mathbf{X}(s), t) \delta(\mathbf{x} - \mathbf{X}(s, t)) dV \quad (3)$$

where  $\mathbf{x}$  and  $\mathbf{X}$  represent the Euler coordinates of the fluid fields (entire computational domain) and the IB points (Lagrangian coordinate of the solid boundary), respectively.  $F_i$  is the solid boundary force density.  $\delta(\mathbf{x} - \mathbf{X}(s, t))$  is the smooth delta function, which is expressed as

$$\delta_h(\mathbf{x}) = \frac{1}{h^3} \phi\left(\frac{x}{h}\right) \phi\left(\frac{y}{h}\right) \phi\left(\frac{z}{h}\right) \quad (4)$$

where  $\phi(r)$  can be written as

$$\phi(r) = \begin{cases} 1/8(3-2|r|+\sqrt{1+4|r|-4r^2}), & 0 \leq |r| < 1 \\ 1/8(5-2|r|+\sqrt{-7+12|r|-4r^2}), & 1 \leq |r| < 2 \\ 0, & 2 \leq |r| \end{cases} \quad (5)$$

where  $h$  is local Euler grid scale.

In the present study, the dynamic model of Gemanio *et al.* (1991) is adopted to model the sub-grid stress (SGS),

$$\tau_{ij} - \frac{\delta_{ij}}{3} \tau_{kk} = -2\mu_t S_{ij} \quad (6)$$

$$\mu_t = \rho C_s \Delta^2 |S| \quad (7)$$

where  $\delta_{ij}$  is the Kronecker delta,  $S_{ij} = (1/2)(\partial u_i / \partial x_j + \partial u_j / \partial x_i)$ ,  $|S| = (S_{ij} S_{ij})^{1/2}$ ,  $\Delta$ , defined as  $(\Delta x \Delta y \Delta z)^{1/3}$ , is the filter width and the mesh size is a parameter of the filtering operator. For the dynamic model, the model coefficient, CD, is allowed to be a function of space and time. Following Lilly (1992), the coefficient is obtained using the least-squares approach.

With the definition of the eddy viscosity, Eq. (2) can be expressed as

$$\begin{aligned} \frac{\partial \rho u_i}{\partial t} + \frac{\partial(\rho u_i u_j)}{\partial x_j} = & -\frac{\partial p}{\partial x_i} + f_i \\ & + \frac{\partial}{\partial x_j} \left[ (\mu + \mu_t) \left( \frac{\partial u_i}{\partial x_j} + \frac{\partial u_j}{\partial x_i} \right) \right] \end{aligned} \quad (8)$$

The laminar flow equation can be recovered by setting  $\mu_t$  to zero.

## 2.2 Immersed boundary framework with implicit direct-forcing

We consider a generic conservation equation of the form of Eq. (8) and another scalar transport equation when the source terms are omitted in the differential form of the domain  $\Omega$

$$\frac{\partial \varphi}{\partial t} + \nabla \cdot \mathbf{M} = 0 \quad (9)$$

where  $\varphi$  represents a conserved quantity such as  $\rho u$ ,  $\rho v$ ,  $\rho w$ ,  $\rho k$ ,  $\rho \varepsilon$  and  $\mathbf{M}$  is a flux function, which can be expressed as

$$\mathbf{M} = \rho \mathbf{u} \varphi + \mathbf{I} p - \Gamma \nabla \varphi \quad (10)$$

where  $\Gamma$  is a generalised diffusive term (e.g., in momentum Eq. (8),  $\Gamma = (\mu + \mu_t)/\rho$  represents the effective kinematic viscosity) and  $\mathbf{I}$  is the identity tensor.

Eq. (9) can be discretised in time from step  $t_n$  to  $t_{n+1}$  (with time-step size  $\Delta t = t_{n+1} - t_n$ ) in the following form

$$\frac{\mathbf{u}' - \mathbf{u}^n}{\Delta t} = \nabla \cdot \mathbf{M}(\mathbf{u}, p) \quad (11)$$

The divergence-free condition, Eq. (1), is enforced by a fractional-step method with the intermediate velocity

$$\frac{\mathbf{u}^* - \mathbf{u}^n}{\Delta t} = \nabla \cdot \mathbf{M}(\mathbf{u}, p) \quad (12)$$

For pressure projection, a Poisson equation,

$$\nabla^2 \phi = -\nabla \cdot \mathbf{u}^* \quad (13)$$

is solved, leading to a divergence-free velocity field

$$\mathbf{u}' = \mathbf{u}^n - \nabla \phi \quad (14)$$

Finally, the pressure is updated by

$$p^{n+1} = p^n + \frac{\phi}{\Delta t} \quad (15)$$

Now we recover the source term,  $\mathbf{f}$ , and the time discretisation of Eq. (8) by subtracting Eq. (11)

$$\frac{\mathbf{u}^{n+1} - \mathbf{u}'}{\Delta t} = \mathbf{f} \quad (16)$$

In conventional IBM, the force density,  $\mathbf{f}$ , is determined in advance and then the corrected velocity,  $\mathbf{u}^{n+1}$ , can be obtained. However, there is no guarantee that the velocity at the IB point interpolated from this corrected velocity always satisfies the no-slip boundary condition. This drawback can be overcome by the present method. The basic idea of our method is that the force density,  $\mathbf{f}$ , is considered as an unknown, which is evaluated implicitly in such a way that the velocity at the IB point interpolated from the corrected velocity,  $\mathbf{u}^{n+1}$ , at the Eulerian grids equals the given velocity of the IB point. By applying the forward Euler method to approximate the

temporal derivative in Eq. (16), it is clear that adding a forcing term,  $\mathbf{f}$ , is equivalent to making a correction,  $\Delta\mathbf{u} = \mathbf{u}^{n+1} - \mathbf{u}'$ , in the velocity field. Suppose that the immersed boundary is represented by a set of IB points,  $\mathbf{X}_{IB}^i$  ( $i = 1, 2, \dots, M$ ), and that the fluid field is discretised by a fixed uniform Cartesian mesh,  $\mathbf{x}_j$  ( $j = 1, 2, \dots, N$ ), with mesh spacing  $\Delta x = \Delta y = \Delta z = h$ . Furthermore, we define two functions,  $C_{ji}$  and  $D_{ij}$ , which represent the interpolation and distribution functions, respectively

$$C_{ji} = C(\mathbf{X}_{IB}^i - \mathbf{x}_j) = \frac{1}{h^3} \phi\left(\frac{X_{IB}^i - x_j}{h}\right) \phi\left(\frac{Y_{IB}^i - y_j}{h}\right) \phi\left(\frac{Z_{IB}^i - z_j}{h}\right) \quad (17)$$

$$D_{ij} = D(\mathbf{x}_j - \mathbf{X}_{IB}^i) = \frac{1}{h^3} \phi\left(\frac{x_j - X_{IB}^i}{h}\right) \phi\left(\frac{y_j - Y_{IB}^i}{h}\right) \phi\left(\frac{z_j - Z_{IB}^i}{h}\right) \quad (18)$$

Note that the distribution function,  $C_{ji}$ , maps the physical field from the IB points to the Cartesian grids, On the other hand, the interpolation function,  $D_{ij}$ , projects the physical field from the Cartesian grids back to the IB points.

Note from Eq. (3) that the force density,  $\mathbf{f}$ , at the Eulerian point is distributed from the boundary force,  $\mathbf{F}$ , through the Dirac delta function interpolation. Eq. (3) can be written in discrete form as

$$\mathbf{f}(\mathbf{x}_j, t) = \sum_i C_{ji} \mathbf{F}(\mathbf{X}_{IB}^i, t) \Delta V_i \quad (i = 1, 2, \dots, M; j = 1, 2, \dots, N) \quad (19)$$

where  $\Delta V_i$  is the  $i$ th segment boundary discrete volume. According to the suggestion of Uhlmann [32], these volumes should form a thin shell of thickness equal to one mesh width around each IB point.

Substituting Eq. (18) into Eq. (15), we have

$$\Delta\mathbf{u}(\mathbf{x}_j, t) = \sum_i C_{ji} \mathbf{F}(\mathbf{X}_{IB}^i, t) \Delta V_i \quad (i = 1, 2, \dots, M; j = 1, 2, \dots, N) \quad (20)$$

It is noted that the unknowns in Eq. (20) are the boundary forces. To satisfy the no-slip boundary condition, the velocity at the IB point interpolated from the corrected fluid velocity field via the smooth delta function,  $D_{ij}$ , must be equal to the boundary velocity,  $\mathbf{U}(\mathbf{X}_{IB}^i, t)$ , at the same position

$$\mathbf{U}(\mathbf{X}_{IB}^i, t) = \sum_j D_{ij} \mathbf{u}^{n+1}(\mathbf{x}_j, t) h^3 \quad (j = 1, 2, \dots, N; i = 1, 2, \dots, M) \quad (21)$$

Here,  $\mathbf{u}^{n+1}(\mathbf{x}_j, t)$  is the corrected velocity at the  $j$ th Eulerian grid point, expressed as the sum of predicted velocity,  $\mathbf{u}'(\mathbf{x}_j, t)$ , and the velocity correction,  $\Delta\mathbf{u}(\mathbf{x}_j, t)$ , namely,

$$\mathbf{u}(\mathbf{x}_j, t) = \mathbf{u}'(\mathbf{x}_j, t) + \Delta\mathbf{u}(\mathbf{x}_j, t) \quad (22)$$

Substituting Eqs. (22) and (20) into Eq. (21) yields

$$\begin{aligned} \mathbf{U}(\mathbf{X}_{IB}^i, t) &= \sum_j \mathbf{u}'(\mathbf{x}_j, t) D_{ij} h^3 \\ &+ \sum_j \sum_i D_{ij} \Delta V_i C_{ji} \mathbf{F}(\mathbf{X}_{IB}^i, t) \Delta t h^3 \quad (i = 1, 2, \dots, M; j = 1, 2, \dots, N) \end{aligned} \quad (23)$$

The equation system for the boundary force has now been formed and can be further written in the following matrix form as

$$\mathbf{AX} = \mathbf{B} \quad (24)$$

where

$$\mathbf{A} = \Delta t h^3 \begin{bmatrix} D_{11}\Delta V_1 & D_{12}\Delta V_1 & \cdots & D_{1N}\Delta V_1 \\ D_{21}\Delta V_2 & D_{22}\Delta V_2 & \cdots & D_{2N}\Delta V_2 \\ \vdots & \vdots & \ddots & \vdots \\ D_{M1}\Delta V_M & D_{M2}\Delta V_M & \cdots & D_{MN}\Delta V_M \end{bmatrix} \begin{bmatrix} C_{11} & C_{12} & \cdots & C_{1M} \\ C_{21} & C_{22} & \cdots & C_{2M} \\ \vdots & \vdots & \ddots & \vdots \\ C_{N1} & C_{N2} & \cdots & C_{NM} \end{bmatrix} \quad (25)$$

$$\mathbf{B} = \begin{bmatrix} \mathbf{U}_{IB}^1 \\ \mathbf{U}_{IB}^2 \\ \vdots \\ \mathbf{U}_{IB}^M \end{bmatrix} - h^3 \begin{bmatrix} D_{11} & D_{12} & \cdots & D_{1N} \\ D_{21} & D_{22} & \cdots & D_{2N} \\ \vdots & \vdots & \ddots & \vdots \\ D_{M1} & D_{M2} & \cdots & D_{MN} \end{bmatrix} \begin{bmatrix} \mathbf{u}'_1 \\ \mathbf{u}'_2 \\ \vdots \\ \mathbf{u}'_N \end{bmatrix} \quad (26)$$

$$\mathbf{X} = \begin{bmatrix} \mathbf{F}_{IB}^1 \\ \mathbf{F}_{IB}^2 \\ \vdots \\ \mathbf{F}_{IB}^M \end{bmatrix} \quad (27)$$

and  $\mathbf{U}_{IB}^i$  and  $\mathbf{u}'_j$  are abbreviations for  $\mathbf{U}(\mathbf{X}_{IB}^i, t)$  and  $\mathbf{u}'(x_j, t)$ , respectively. It can be observed that the elements of coefficient matrix  $\mathbf{A}$  are only related to the coordinate information of the IB points and their adjacent Eulerian points. The equation system (24) is solved by the Gauss-Jordan iterative method; the unknown boundary forces,  $\mathbf{F}(\mathbf{X}_{IB}^i, t)$ , at all IB points are obtained simultaneously and then substituted into Eqs. (20) and (22) to calculate the velocity correction,  $\Delta \mathbf{u}(\mathbf{x}_j, t)$ , and the corrected velocity,  $\mathbf{u}^{n+1}(\mathbf{x}_j, t)$ .

### 2.3 Wall model in a turbulent boundary layer

For any random fluid point (in Fig. 1, fluid point A), we can find a projected point on the IB boundary (in Fig. 1, projected point B) when the topology of the boundary is described using the methodology proposed by Udaykumar *et al.* (1997, 1999). We use a linear interpolation of its two neighbours to obtain an approximate boundary force density,  $\mathbf{F}(\mathbf{X}_{IB}^B, t)$ ; then  $\mathbf{F}(\mathbf{X}_{IB}^B, t)$  can be decomposed along the tangential and normal directions of the wall to  $\mathbf{F}_\tau(\mathbf{X}_{IB}^B, t)$  and  $\mathbf{F}_n(\mathbf{X}_{IB}^B, t)$ , respectively. We know that  $\mathbf{F}(\mathbf{X}_{IB}^i, t)$  is the boundary force density acting on the fluid, and owing to the fact that action and reaction are equal and opposite, it is obvious that the force exerted by the fluid on the boundary should be  $-\mathbf{F}(\mathbf{X}_{IB}^i, t)$  at each IB point. Since it is difficult to calculate the friction force in the present IB method, in this study, the wall shear stress can be well approximated as  $\tau_w = -\mathbf{F}_\tau h$ , where  $\mathbf{F}_\tau$  is the abbreviation for  $\mathbf{F}_\tau(\mathbf{X}_{IB}^i, t)$ . The wall-normal distance,  $y$ , is approximately normalised as

$$y_w^+ = y\rho u_\tau / \mu = y\sqrt{\tau_w / \rho} / \nu \quad (28)$$

where  $y$  is the normal distance from the Eulerian grid points to the solid boundary, namely, the distance between points A and B and  $u_\tau$  is the wall friction velocity. The following simplified turbulent boundary layer equations can now be solved

$$\frac{\partial \rho u_i}{\partial t} + \frac{\partial(\rho u_i u_j)}{\partial x_j} = -\frac{\partial p}{\partial x_i} + \frac{\partial}{\partial y} \left[ (\mu + \mu_t) \frac{\partial u_i}{\partial y} \right] + f_i \quad i=1,3 \quad (29)$$

where  $y$  denotes the direction normal to the wall and  $i$  identifies the wall-parallel directions (1 and 3). The eddy viscosity,  $\mu_t$ , is obtained from a mixing-length model with near-wall damping, as done by Wang and Moin (2002):  $\frac{\mu_t}{\mu} = \kappa y_w^+ (1 - e^{-y_w^+/A})^2$ . The boundary conditions for the

turbulent boundary layer equations are given by the unsteady outer-layer solution at the first grid node outside the wall layer and the no-slip condition at  $y=0$ , where  $\kappa$  is von Karman's constant and  $A$  is an integration constant, where  $\kappa=0.4$ ,  $A=19$  is adopted.

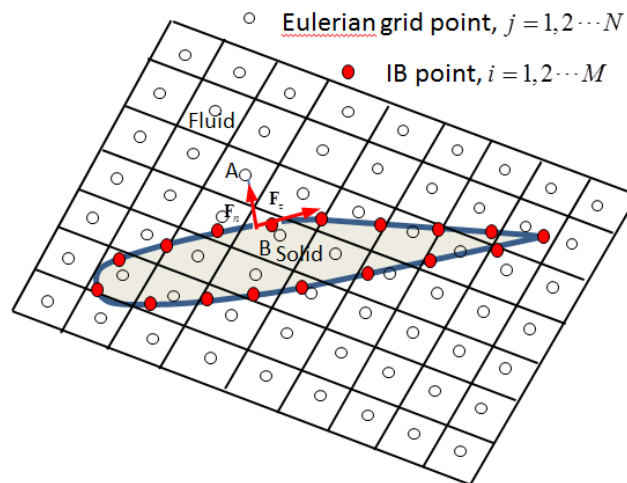


Fig. 1 Schematic description of the implicit direct-forcing IB method and the wall shear stress interpolation in a wall model for moving boundary problems

### 3. Turbulent flow in a Francis turbine passage with a uniform operating guide vane

#### 3.1 Computational setup

As a numerical example, we examine a runner blade in a test Type-HLA551-LJ-43 Francis hydroturbine model. The computational domain comprising the distributor (stay vanes and guide vanes) and runner is shown in Fig. 2 and consists of one stay vane, one guide vane and one runner blade. The distributor computational domain corresponds to an inter-blade channel that is bounded upstream by a cylindrical patch, A-A, and downstream by a conical patch, B-B. The distributor

inlet section corresponds to the spiral casing outlet section, while the outlet section is conventionally considered to be the distributor-runner interface. The runner computational domain also corresponds to an inter-blade channel that is bounded upstream by a conical patch (wrapped on the same conical surface as the distributor outlet), then reaches across the runner middle axis, C-C, and is extended downstream up to the draft tube inlet of radius D-D. The geometry is normalised with half of the external diameter of the runner blade,  $R_{ref}=0.225$  m. The mean chord dimension,  $L$ , of the runner blade passage (streamwise dimension) is as  $L/R_{ref}=0.724$ , the mean blade-pitch dimension as  $y/R_{ref}=0.46$  and the mean spanwise dimension of the blade passage as  $z/R_{ref}=2.06$ . The mean coming flow velocity at the inlet of the distributor domain (A-A) passage is defined as the reference velocity,  $U_{ref}=0.1$  m/s. The flow Reynolds number is defined as  $Re=U_{ref}L/\nu^f=1.62\times 10^4$ . The attack angle,  $\alpha$ , of the guide vane relative the blade is  $0^\circ$  initially and defined as

$$\begin{cases} \alpha = \omega t & 0 \leq t < T/2 \\ \alpha = \omega(T-t) & T/2 \leq t \leq T \end{cases} \quad (30)$$

where  $\omega=6^\circ/s$  is the rotating angular velocity of the guide vane and  $T=20$  s is its swirling period. The computational time step is  $5.0\times 10^{-3}$  s and the total computational time is five periods, consuming a CPU time of nearly six months.

There are 29,305 hexahedral fluid elements generated first in the guide vane rotating zone and then calculated in the other domains in turn. The surface of the guide vane is discretised using 1,476 quadrilateral mesh nodes representing the immersed boundary, and 11,160 nodes are distributed over one side of the blade surfaces (averaging 90 points in the streamwise direction and 124 points in the spanwise direction).

The computational boundary conditions are shown in Fig. 2 and presented as follows. A uniform velocity field that is normal at the inflow section is imposed on the distributor inlet section. The turbulence quantities (a turbulence intensity of 4% and a turbulence length scale of  $l=0.07R$ , where  $R$  is the hydroradius of the distributor inlet section) are prescribed on the inflow section of the distributor, the free outflow condition is specified on the runner outlet (draft tube inlet), the periodic conditions are imposed on the pitchwise periodic boundary, and no-slip wall conditions are imposed on the stay vane, runner blade and distributor upper and lower rings as well as on the crown and band surfaces of the runner blade.

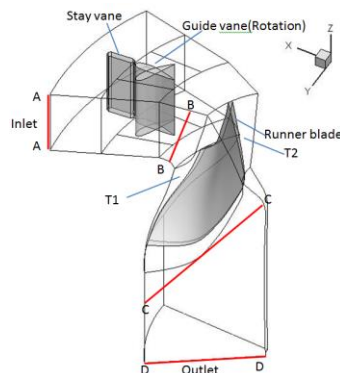


Fig. 2 Description of the computational zone with a rotating guide vane in the transition process of a Francis turbine

### 3.2 Numerical results

The results described in this section are from the computational data of the fifth period. The drag coefficient is defined as

$$C_D = \frac{F_D}{\frac{1}{2} \rho U_{Ref}^2 L^2} \quad (31)$$

The drag can be computed from the force along the cylinder interface as

$$F_D = \int_{\Gamma} F_x h dS \quad (32)$$

where  $F_x$  is the  $x$ -component of the solid boundary force. The lift coefficient is defined as

$$C_L = \frac{F_L}{\frac{1}{2} \rho U_{Ref}^2 L^2} \quad (33)$$

The lift can be computed from the force along the cylinder interface as

$$F_L = \int_{\Gamma} F_y h dS \quad (34)$$

where  $F_y$  is the  $y$ -component of the solid boundary force. The axis coefficient,  $C_z$ , is defined as

$$C_{axis} = \frac{F_{axis}}{\frac{1}{2} \rho U_{Ref}^2 L^2} \quad (35)$$

The force along the rotating axis ( $z$ -axis) can be computed as

$$F_{axis} = \int_{\Gamma} F_z h dS \quad (36)$$

where  $F_z$  is the  $z$ -component of the solid boundary force. The moment coefficient is defined as

$$C_M = \frac{M}{\frac{1}{2} \rho U_{Ref}^2 L^3} \quad (37)$$

The force moment can be computed as

$$M = \int_V \mathbf{F} \times \mathbf{r} dV \quad (38)$$

where  $\mathbf{F}$  is the boundary force density of an immersed solid and  $\mathbf{r}$  is the distance between the IB points and rotating axis of the guide vane. In the case of the runner blade,  $\mathbf{F}$  is the fluid stress and  $\mathbf{r}$  is the distance between centre of the grid cell and the shaft of the unit.

Fig. 3 shows the drag, lift and axis coefficients of a guide vane in a rotating period. First, when

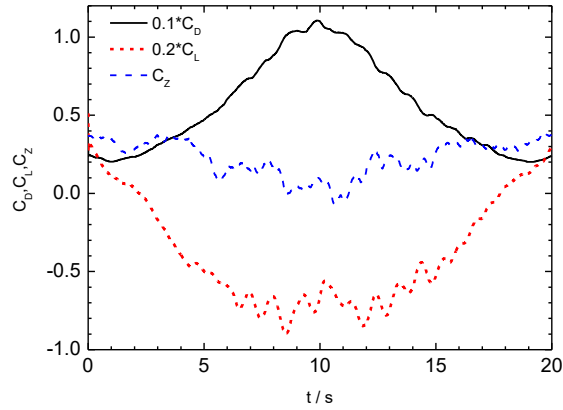


Fig. 3 The drag, lift and axis coefficients of a guide vane over its rotating period

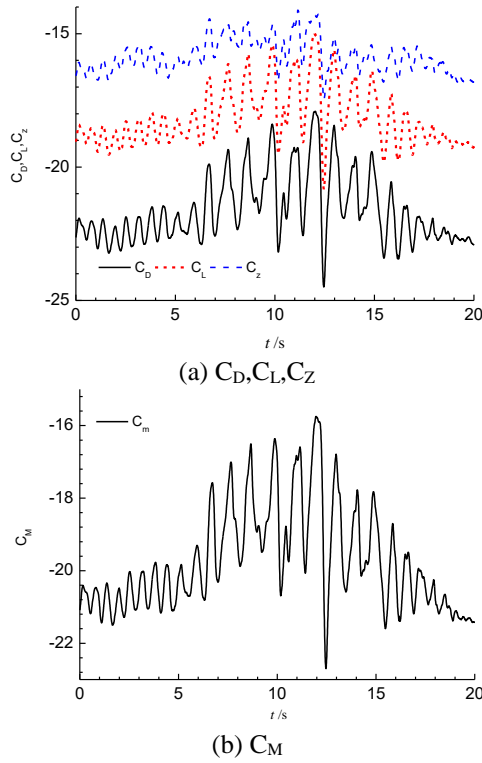


Fig. 4 The drag, lift, axis and moment coefficients of a runner blade during a rotating period of the guide vane

the attack angle is equal to zero, the drag, lift and axis coefficients are all positive. The drag coefficient increases continuously with the attack angle, attaining a maximum value when the attack angle is nearly  $60^\circ$  (maximum attack angle) that is about four times of the value when attack angle is nearly  $0^\circ$ . However, the lift coefficient decreases with the increase in attack angle and becomes negative when the attack angle is larger than  $13.2^\circ$ , before continuing to decrease to a

minimum when the attack angle is near  $58.4^\circ$ . The change of the axis coefficient is between zero and 0.4 and less than the drag and lift coefficients. We can also see that the drag, lift and axis coefficients are local fluctuations when the attack angle is larger than  $40^\circ$ , which may be attributed to the instability of the flow as well as tip vortex shedding at large attack angles. From the force coefficient, it is concluded that the shear stress and moment about the rotating axis of the guide vane is also maximised when the attack angle is nearly maximal; so much more care is needed to operate in a transition process of a hydraulic turbine.

Fig. 4 shows the drag, lift, axis and moment coefficients of a runner blade in a rotating period of a guide vane. From this figure, it can be seen that the coefficients all pulsate along with the change of attack angle of guide vane. It is also apparent that the local average value and the pulsating amplitude is enlarged along with the increase of the attack angle of the guide vane, which may be caused by two mainly reasons, one is due to the difference of the tailing vortex structure entered into the runner blade passage under different attack angles of the guide vane, another is due to the difference of eddy scales induced by curvature of the blade wall itself. From the outstanding wakening character of the force coefficient, it is concluded that the runner blade is loaded by the pulsating force, resulting in a local rupture of the runner blade and that the shaft of the unit will be loaded by the unbalanced force along the radial and axial directions.

Fig. 5 shows the volume-weighted average vorticity on the runner blade passages along the streamwise, pitchwise and spanwise directions against attack angle in a rotating period of the guide vane. The volume-weighted average of a quantity is computed by dividing the summation of the product of the selected field variable,  $\phi$ , and the cell volume,  $V_i$ , by the total volume of the cell zone,  $V$ , which is defined by  $\int_V \phi dV / V = \sum_{i=1}^n \phi_i V_i / V$ . From these figures, it can be seen that the streamwise, pitchwise and spanwise vorticities are different between the T1 and T2 cell zones, which is attributed to the different positions relative to the upstream guide vane. It also can be seen that the streamwise, pitchwise and spanwise vorticities show large pulsation; furthermore, pulsating amplitude gradually increases as the attack angle increases, verifying that larger attack angles of the guide vane may result in more intense vortices and may finally induce stronger vibration of the runner.

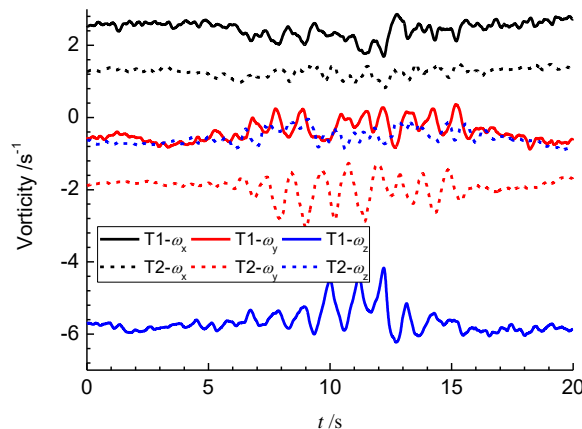


Fig. 5 The volume-weighted average vorticity on the runner blade passages along the streamwise, pitchwise and spanwise directions against the attack angle in a rotating period of the guide vane

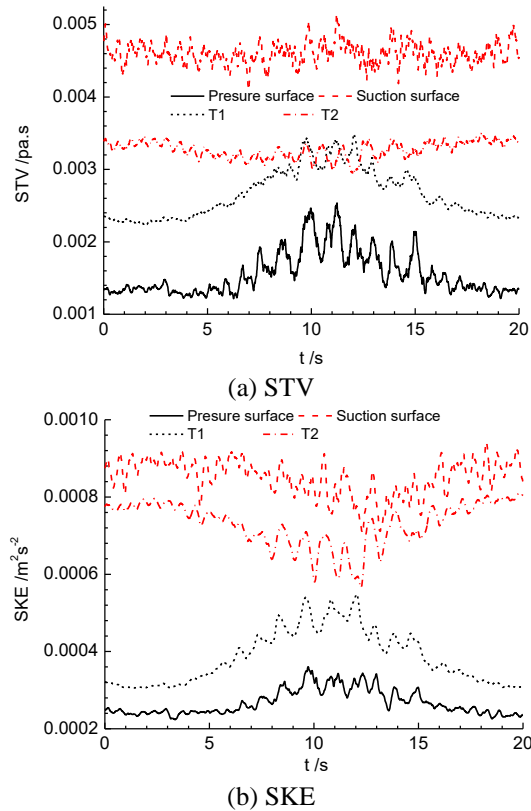


Fig. 6 Volume-weighted average sub-grid turbulent viscosity (STV) and sub-grid kinematic energy (SKE) on the runner blade passages and the surface-weighted average STV and SKE on the runner blade surface against the attack angle over a rotating period of the guide vane

Fig. 6 shows the volume-weighted average sub-grid turbulent viscosity (STV) and sub-grid kinematic energy (SKE) on the runner blade passage as well as the surface-weighted average STV and SKE on the runner blade surface against attack angle in a rotating period of the guide vane. The area-weighted average of a quantity is computed by dividing the summation of the product of the selected field variable,  $\phi$ , and facet area,  $A_i$ , by the total area,  $A$ , of the surface, which is defined by  $\int_A \phi dA / A = \sum_{i=1}^n \phi_i A_i / A$ . From Fig. 9(a), it is shown that the maximum STV is nearly 5.2 times the molecular viscosity. We can also see that the surface-weighted average STV near the suction surface is larger than that near the pressure surface at all attack angles; however, the volume-weighted average STV in the T1 cell zone is close to that in the T2 cell zone when the attack angle is larger than  $54^\circ$  and is much lower than that when the attack angle is below  $54^\circ$ . The pulsating amplitudes of STV in the T1 cell and near to the pressure surface gradually increase with the attack angle; however, those in the T2 cell and near to the suction surface increase little with the attack angle changing. Furthermore, the figure shows that the pulsating amplitude of the surface-weighted average STV near the runner wall surface is larger than the volume-weighted average STV in the runner passage, which is in agreement with the physical reality. From Fig. 9(b), we can see that the surface-weighted average SKE near the suction surface and the volume-weighted

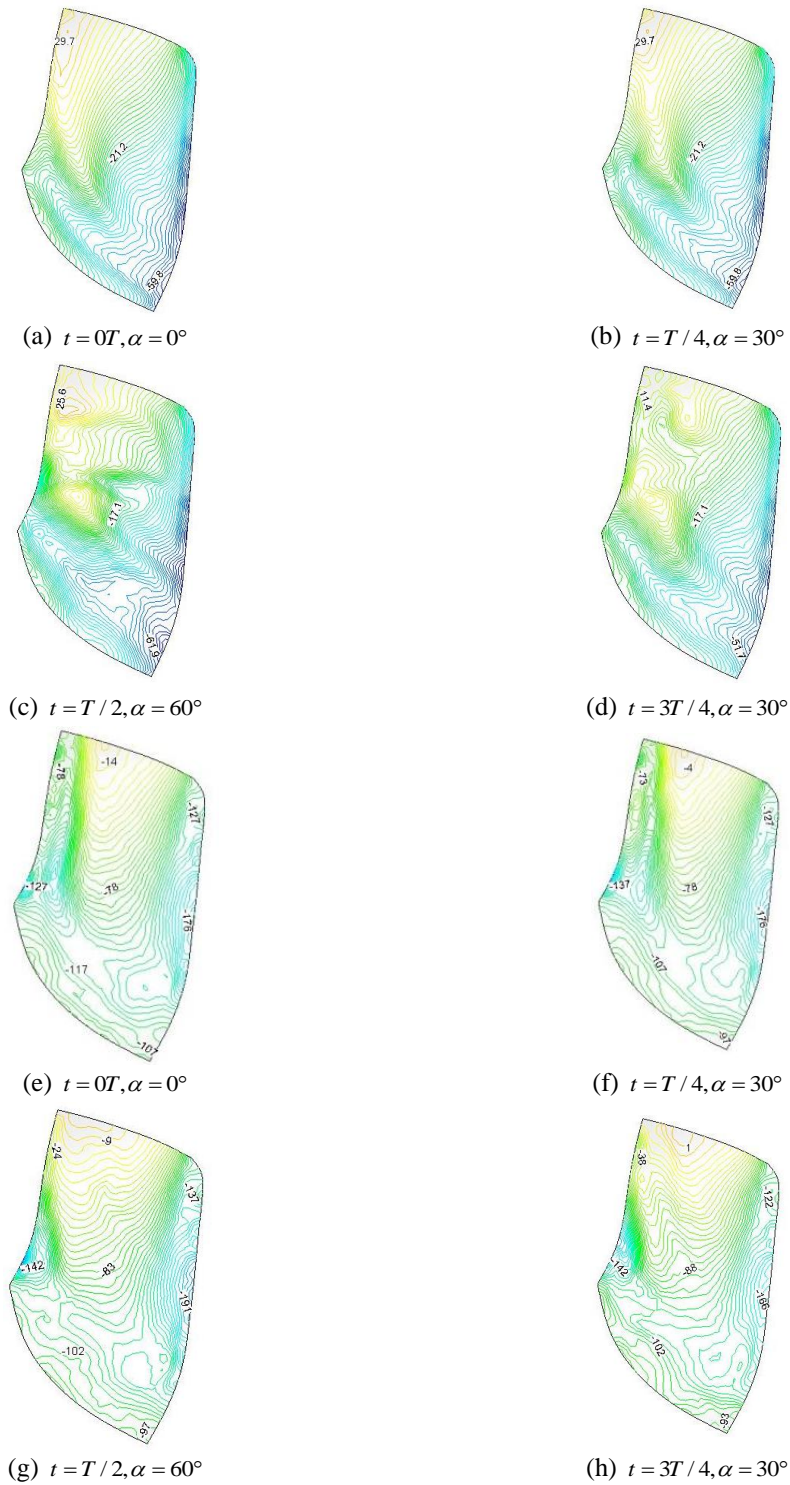


Fig. 7 Contour lines of the pressure. (a)-(d) pressure surface, 60 contour levels in the range from -70 Pa to 50 Pa; (e)-(h) suction surface, 60 contour levels in the range from -240 Pa to 50 Pa

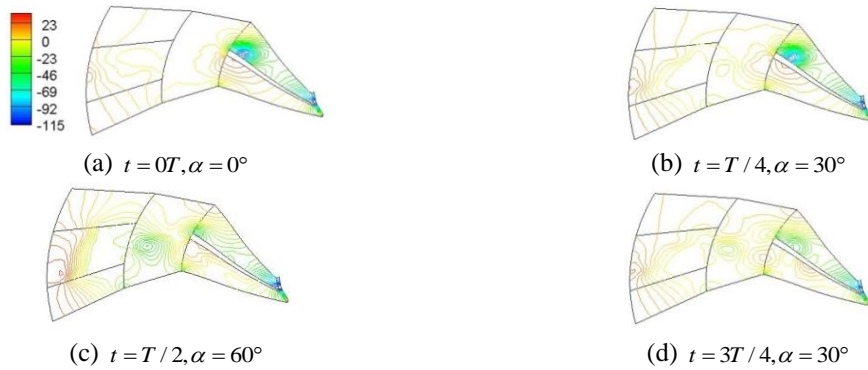


Fig. 8 Contour lines of the pressure at a section across the middle of the guide vane in spanwise direction. 40 contour levels in the range from -115 Pa to 35 Pa

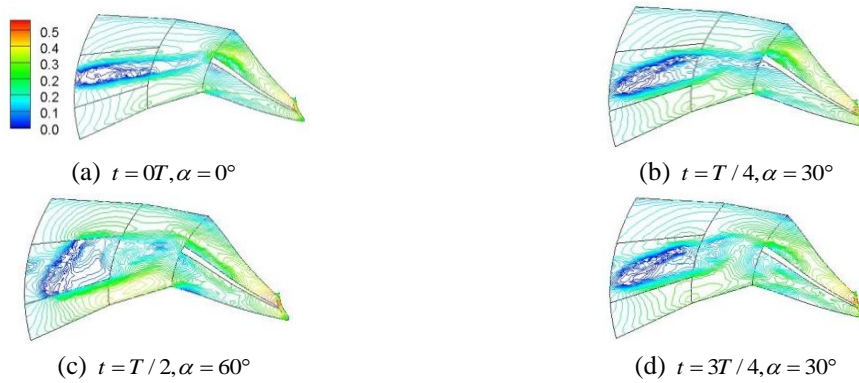


Fig. 9 Contour lines of the velocity magnitude at a section across the middle of the guide vane in the spanwise direction. 40 contour levels in the range of 0 to 0.5

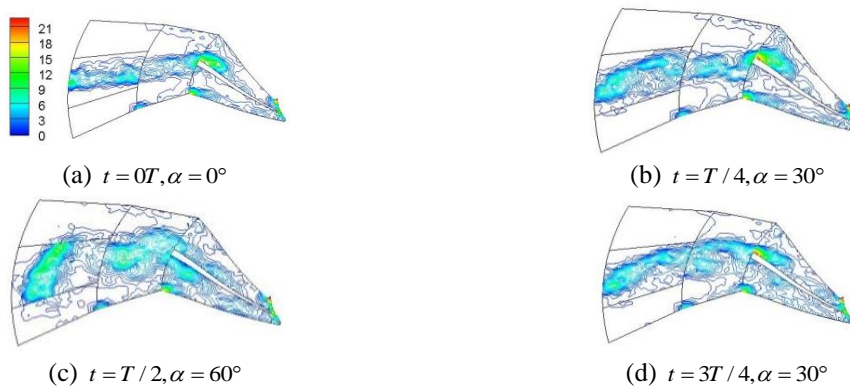


Fig. 10 Contour lines of the ratio of eddy viscosity to molecular viscosity  $\mu_t/\mu$  in a section across the middle of a guide vane in the spanwise direction. 46 contour levels in the range of 0 to 23

average SKE in the T2 cell zone are globally rising; however, that near the pressure surface and that in T1 cell zone decrease globally with the increase of the attacking angle. Moreover, the surface-weighted average SKE near the suction surface is close to 3 times that near the pressure

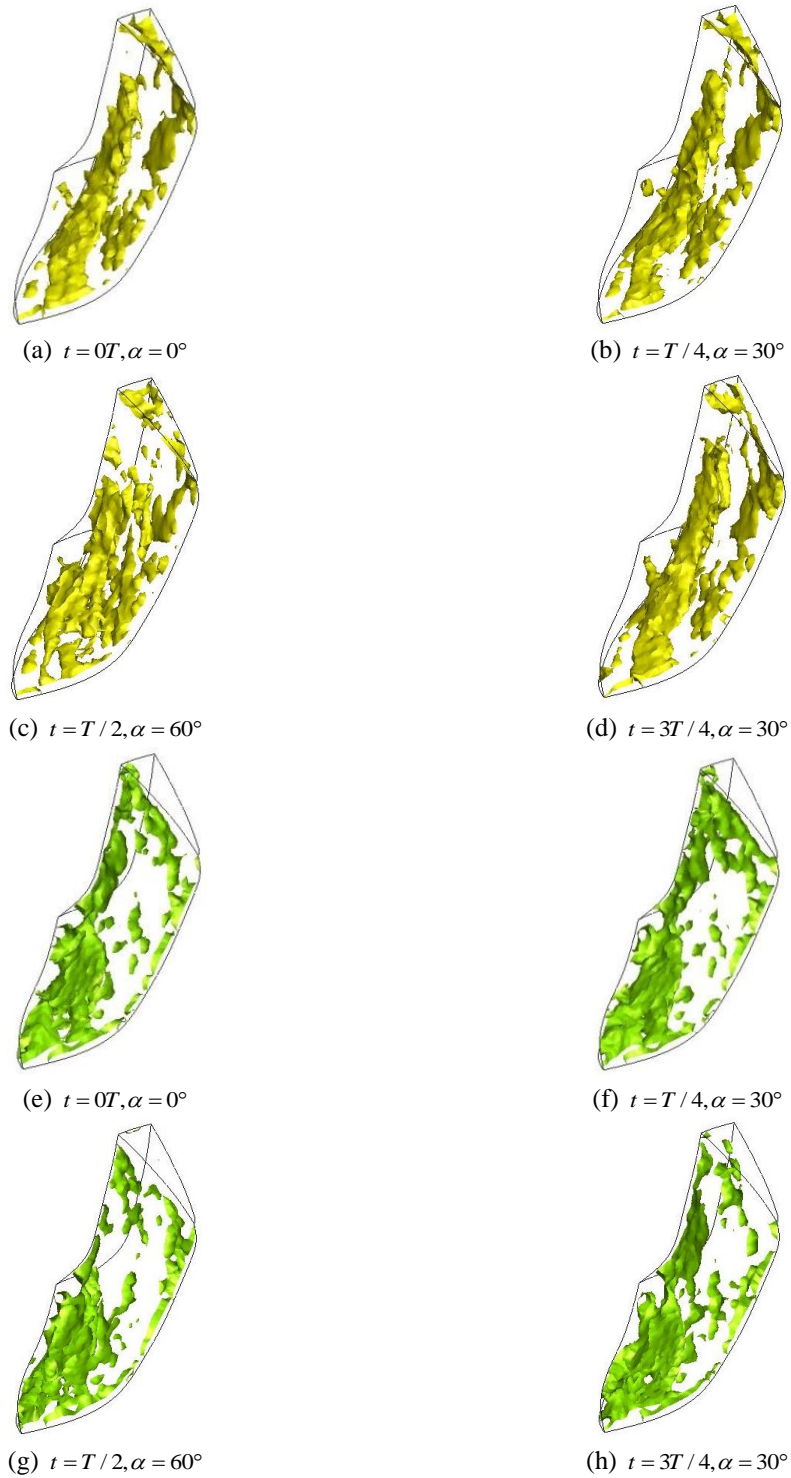


Fig. 11 Instantaneous iso-surfaces of pitchwise and spanwise vorticity in the blade passage over a period. (a)-(d)  $\omega_y = 5 \text{ s}^{-1}$ ; (e)-(h)  $\omega_y = -5 \text{ s}^{-1}$ . (A)-(D)  $\omega_z = 15 \text{ s}^{-1}$ ; (E)-(H)  $\omega_z = -20 \text{ s}^{-1}$

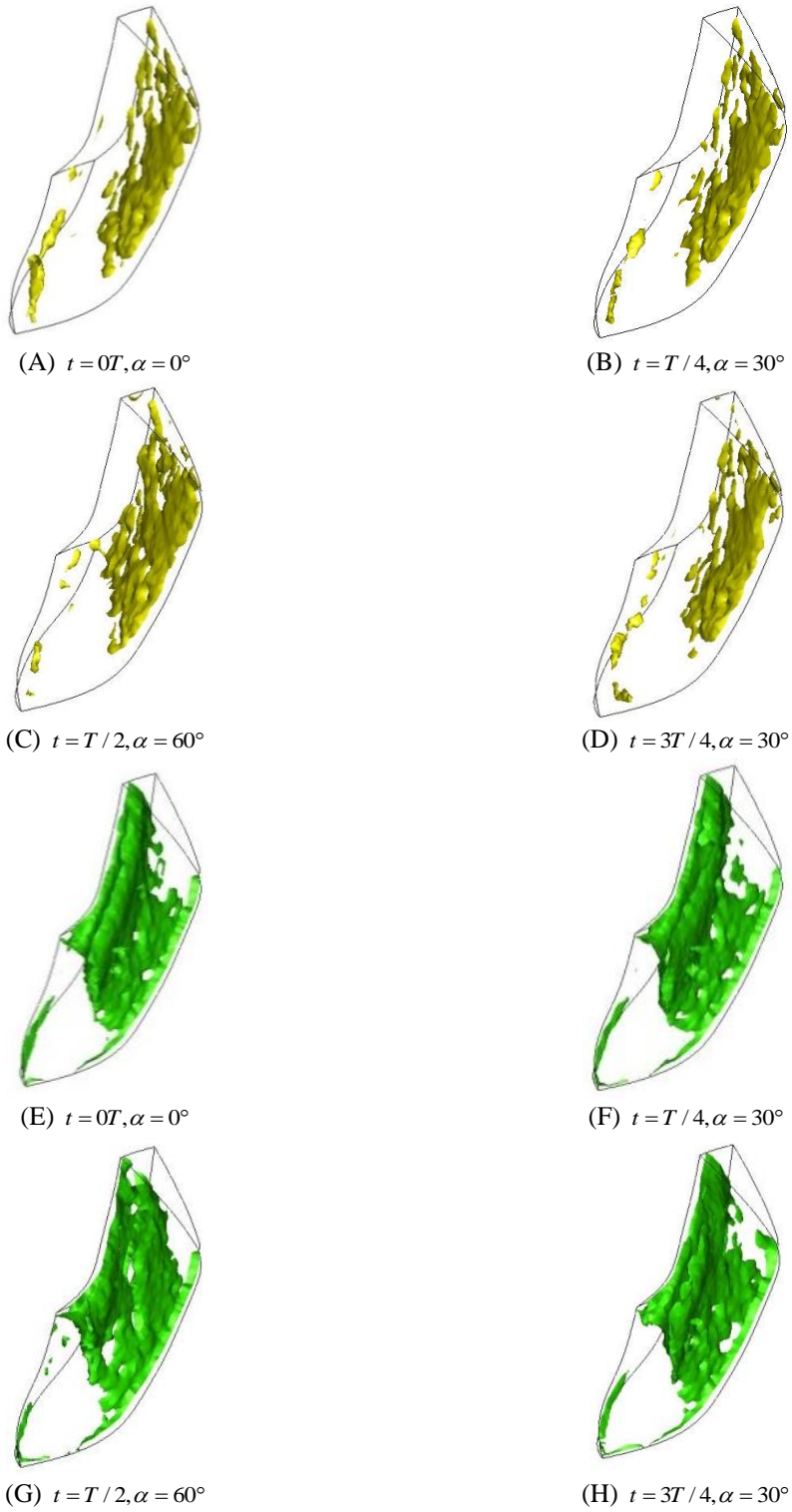


Fig. 11 Continued

surface, and the volume-weighted average SKE in the T2 cell zone is also larger than that in the T1 cell zone.

Fig. 7 shows the static pressure distribution on the pressure and suction surfaces in a rotating period of a guide vane. From Fig. 10(a)-(b), it can be seen that the pressure attains a maximum near the leading end of the blade passage on the pressure surface, which gradually decreases along the streamline up to a minimum at the trailing edge of the blade passage, and as a whole, the pressure contour line is uniform and two evident pressure stripes are formed. One is the high-pressure stripe near the leading edge of the runner blade, and the other is the low-pressure stripe along the downer band. However, in Fig. 10(c)-(d), the uniform pressure contour lines are broken by local a high-pressure zone with the change in attack angle. The contours of the static pressure on the suction side are messier than those on the pressure side. The pressure attains a local minimum at the leading of the blade passage and soon attains a maximum on the midpoint of the blade passage near the crown region, suggesting that there is very closed to a strong vortex formation in the leading zones.

Fig. 8 shows the contour lines of the pressure in the section across the middle of the guide vane in the spanwise direction. There is a low-pressure zone at the leading edge on the suction surface in Fig. 11(a)-(b), which verifies that there is a strong swirling vortex along the suction surface. However, the low-pressure zone along the suction surface is not obvious, but a local low-pressure zone comes into being behind the guide vane when the attack angle is  $60^\circ$ .

Fig. 9 shows the contour lines of the velocity in the section across the middle of the guide vane in the spanwise direction. From this figure, it can be seen that the position and the intensity of the velocity band in flowing passage evolve with change in the attack angle; also, which enter into the runner blade passage and finally result in the large different of pressure and velocity distribution as well as the vortex structure in runner blade.

Fig. 10 shows the contour lines of the ratio of eddy viscosity to molecular viscosity,  $\mu_t/\mu$ , in the section across the middle of the guide vane in the spanwise direction. It is shown that the STV in the trailing wake zone is higher and that the high stripe of STV directly extends into the blade passage, thereby verifying that the tailing vortex of the guide vane upstream will significantly affect the fluid patters of the blade passage. At the same time, eddy viscosity is maximal at the leading edge of the suction blade surface due to the strong swirling vortex when the attack angle is close to  $30^\circ$ .

Fig. 11 shows the instantaneous iso-surfaces of the pitchwise and spanwise vorticities in the blade passage at different times in a rotating period of the guide vane. This figure clearly shows how the swirling flow structures and vortex pairs rotating in clockwise and anticlockwise directions come into being in the runner blade passage. It is also shown that the vortex structure is different at different attack angles, implying that the flow patterns are considerably affected by the distorted wakes from the trailing vortex of the guide vane upstream due to the change in the attack angle of guide vane.

#### 4. Conclusions

In this study a coupling mathematical model of the transition process in a Francis turbine comprising complex turbulent flow and moving boundary problems with rotating rigid guide vanes was established using the unsteady Navier-Stokes equation with an additional momentum source term based on an implicit direct-forcing IB method combined with a three-step time-splitting method. The large-eddy simulation was applied in the solver, where the sub-grid stress was

determined by the Smagorinsky-Lilly model. Near the immersed boundaries, the sub-grid stress was determined by a wall model, where the wall shear stress was directly calculated from the Lagrangian force on the immersed boundary. This was simple and easy to implement in a simulation of high-Reynolds number turbulent flow with implicit velocity correction in the IB method.

The spatiotemporal distributions of pressure, velocity, vorticity and turbulent quantities were obtained in one flow passage during a transient process period. The drag and lift coefficients as well as other forces (moments) as functions of attack angle were also obtained. At the same time, analyses of the characteristics of pressure pulsation, velocity stripes and vortex structure at some key parts of flowing passage were undertaken. Furthermore, coupling relations amongst the turbulent flow, the dynamical force (moment) response of the blade and the rotation of the guide vane were obtained.

This research is helpful for improving our understanding of turbulent flow characteristics as well as our ability to operate the opening of a guide vane in a transient process. In the future, the whole flowing passage including all guide vanes in a real-life hydroturbine should be researched in detail.

## Acknowledgements

This work was funded by Research Grants from the Natural Science Foundation of China (Grant Nos. 51479085 and 11262008) and the Fok Ying Tung Education Foundation (No.141120). The authors are grateful for their financial support.

## References

- Alligné, S., Maruzewski, P., Dinh, T., Wang, B., Fedorov, A., Iosfin, J. and Avellan, F. (2010), "Prediction of a Francis turbine prototype full load instability from investigations on the reduced scale model", *IOP Conf. Ser.: Earth Environ. Sci.*, **12**(1), 012025.
- Cherny, S., Chirkov, D., Bannikov, D., Lapin, V., Skorospelov, V., Eshkunova, I. and Avdushenko, A. (2010), "3D numerical simulation of transient processes in hydraulic turbines", *IOP Conf. Ser.: Earth Environ. Sci.*, **12**(1), 012071.
- Chirkov, D., Avdyushenko, A., Panov, L., Bannikov, D., Cherny, S., Skorospelov, V. and Pylev, I. (2012), "CFD simulation of pressure and discharge surge in Francis turbine at off-design conditions", *IOP Conf. Ser.: Earth Environ. Sci.*, **15**, 032038.
- De, J.E., Janssens, N. and Malphet, B. (1994), "Hydro turbine model for system dynamic studies", *Trans. Pow. Syst.*, **9**(4), 1709-1714.
- Germano, M., Piomelli, U., Moin, P. and Cabot, W. (1991), "A dynamic subgrid-scale eddy viscosity model", *Phys. Flu. A*, **3**(7), 1760-1765.
- Gilmanov, A. and Sotiropoulos, F. (2005), "A hybrid Cartesian/immersed boundary method for simulating flows with 3D, geometrically complex, moving bodies", *J. Comput. Phys.*, **207**(2), 457-492.
- Gorla, R.S.R., Pai, S.S. and Blankson, I. (2005), "Unsteady fluid structure interaction in a turbine blade", *Proceedings of the ASME Turbo. Expo.*, Nevada, U.S.A.
- Hasmatuchi, V., Farhat, M. and Roth, S. (2011), "Experimental evidence of rotating stall in a pump-turbine at off-design conditions in generating mode", *J. Flu. Eng.*, **133**(5), 051104.
- Jain, S.V. and Patel, R.H. (2014), "Investigations on pump running in turbine mode: A review of the state-of-the-art", *Renew. Sus. Energy Rev.*, **30**, 841-868.

- Jiang, Y.Y., Yoshimura, S. and Imai, R. (2010), "Quantitative evaluation of flow-induced structural vibration and noise in turbo-machinery by full-scale weakly coupled simulation", *J. Flu. Struct.*, **23**(4), 531-544.
- Kang, S., Lightbody, A., Hill, C. and Sotiropoulos, F. (2011), "High-resolution numerical simulation of turbulence in natural waterways", *Adv. Wat. Res.*, **34**(1), 98-113.
- Keck, H. and Sick, M. (2008), "Thirty years of numerical flow simulation in hydraulic turbomachines", *Acta Mech.*, **201**(1-4), 211-229.
- Li, D., Wang, H. and Xiang, G. (2015), "Unsteady simulation and analysis for hump characteristics of a pump turbine model", *Renew. Energy*, **77**, 32-42.
- Li, J., Yu, J. and Wu, Y. (2010), "3D unsteady turbulent simulations of transients of the Francis turbine", *IOP Conf. Ser.: Earth Environ. Sci.*, **12**(1), 012001.
- Lilly, D.K. (1992), "A proposed modification of the Germano subgrid-scale closure method", *Phys. Flu.*, **4**(3), 633-635.
- Liu, J., Liu, S. and Sun, Y. (2013a), "Three-dimensional flow simulation of transient power interruption process of a prototype pump turbine at pump mode", *J. Mech. Sci. Technol.*, **27**(5), 1305-1312.
- Liu, J., Liu, S. and Sun, Y. (2013b), "Three dimensional flow simulation of load rejection of a prototype pump-turbine", *Eng. Comput.*, **29**(4), 417-426.
- Mittal, R. and Iaccarino, G. (2005), "Immersed boundary methods", *Annu. Rev. Flu. Mech.*, **37**, 239-261.
- Nicolet, C. (2007), "Hydroacoustic modeling and numerical simulation of unsteady operation of hydroelectric systems", Ph.D. Dissertation, EPFL, Lausanne, Switzerland.
- Nicolle, J., Morissette, J.F. and Giroux, A.M. (2012), "Transient CFD simulation of a Francis turbine startup", *IOP Conf. Ser.: Earth Environ. Sci.*, **15**(6), 062014.
- Olimstad, G., Nielsen, T. and Børresen, B. (2012), "Stability limits of reversible-pump turbines in turbine mode of operation and measurements of unstable characteristics", *J. Flu. Eng.*, **134**(11), 111202.
- Peskin, C. (2003), "The immersed boundary method", *Acta Numer.*, **11**, 479-517.
- Peskin, C. (1972), "Flow patterns around heart valves: a numerical method", *J. Comput. Phys.*, **10**, 252-271.
- Sotiropoulos, F. and Yang, X. (2014), "Immersed boundary methods for simulating fluid-structure interaction", *Progr. Aerosp. Sci.*, **65**, 1-21.
- Udaykumar, H.S., Kan, H.C., Shyy, W. and Tran-Son-Tay, R. (1997), "Multiphase dynamics in arbitrary geometries on fixed Cartesian grids", *J. Comput. Phys.*, **137**(2), 366-405.
- Udaykumar, H.S., Mittal, R. and Shyy, W. (1999), "Computation of solid-liquid phase fronts in the sharp interface limit on fixed grids", *J. Comput. Phys.*, **153**(2), 535-574.
- Wang, M. and Moin, P. (2002), "Dynamic wall modeling for large eddy simulation of complex turbulent flows", *Phys. Flu.*, **14**(7), 2043-2051.
- Wang, W.Q., He, X.Q. and Zhang, L.X. (2010), "Strongly coupled simulation of fluid-structure interaction in a Francis hydroturbine", *Int. J. Numer. Meth. Fl.*, **60**(5), 515-538.
- Wang, W.Q., Zhang, L.X. and Guo, Y. (2010), "Turbulent flow simulation using LES with dynamical mixed one-equation subgrid models in complex geometries", *Int. J. Numer. Meth. Fl.*, **63**(5), 600-621.
- Werner, V.N. and Peter, N. (2004), "Goldithal-4X265MW pump turbines in Germany: Special mechanical design features and comparison between stationary and variable speed operation", *Proceedings of the 22nd IAHR Symposium on Hydraulic Machinery and Systems*, Stockholm, Sweden.
- Widmer, C., Staubli, T. and Ledergerber, N. (2011), "Unstable characteristics and rotating stall in turbine brake operation of pump-turbines", *J. Flu. Eng.*, **133**(4), 041101.
- Yin, J., Wang, D. and Keith, W.D. (2014), "Investigation of the unstable flow phenomenon in a pump turbine", *Sci. Chin. (Phys. Mech. Astronom.)*, **57**(6), 1119-1127.
- Zhang, L.X., Wang, W.Q. and Guo, Y. (2010), "Numerical simulation of flow features and energy exchanging physics in near-wall region with fluid-structure interaction", *Int. J. Mod. Phys. B*, **22**(6), 1-19.
- Zhang, X.X. and Cheng, Y.G. (2012), "Simulation of hydraulic transients in hydropower systems using the 1-D-3-D coupling approach", *J. Hydrodyn.*, **24**(4), 595-604.